Aperiodicity is more effective than disorder in localizing electromagnetic waves [Invited]

Luis Razo-López, Geoffroy J. Aubry, Felipe Pinheiro, Fabrice Mortessagne

To cite this version:

Luis Razo-López, Geoffroy J. Aubry, Felipe Pinheiro, Fabrice Mortessagne. Aperiodicity is more effective than disorder in localizing electromagnetic waves [Invited]. Optical Materials Express, 2024, 14 (3), pp.816. 10.1364/OME.514886 . hal-04720814

HAL Id: hal-04720814
https://hal.science/hal-04720814v1

Optical Materials EXPRESS

Aperiodicity is more effective than disorder in localizing electromagnetic waves [Invited]

LUIS A. RAZO-LÓPEZ,[1] GEOFFROY J. AUBRY,[1,3] FELIPE A. PINHEIRO,[2] AND FABRICE MORTESSAGNE[1,4]

[1] Université Côte d'Azur, CNRS, Institut de Physique de Nice (INPHYNI), Nice, France
[2] Instituto de Física, Universidade Federal do Rio de Janeiro, Rio de Janeiro-RJ, 21941-972, Brazil
[3] fabrice.mortessagne@univ-cotedazur.fr
[4] geoffroy.aubry@univ-cotedazur.fr

Abstract: Strong localization of electromagnetic waves in 3D has never been experimentally achieved in uncorrelated disordered systems. By going beyond the paradigm of disordered systems, this goal has been recently reached in deterministic aperiodic planar Vogel spiral arrays in the microwave regime. Here we present a comprehensive description of the experimental details that have been used to observe electromagnetic localization in Vogel spirals beyond 2D. By providing an experimental roadmap to describe microwave transport in Vogel spirals we introduce a novel system platform to demonstrate electromagnetic localization in 3D that outperforms traditional disordered systems for that purpose.

1. Introduction

Interference of matter waves can inhibit classically allowed transport in quantum electronic systems. Anderson demonstrated in his 1958 seminal paper that the existence of uncorrelated disorder in the crystalline lattice can lead to localized wave functions [1]. Due to the localization of electrons, they cannot participate in conduction, leading to a disorder-driven phase transition from metal to insulator. As it typically occurs in phase transitions, Anderson localization (AL) depends on the dimensionality of the system. The scaling theory of localization [2] states that in 1D and 2D systems any disorder is sufficient to localize a wavefunction, whereas in 3D there is a phase transition between a conducting phase (extended states) and an insulating phase (localized states) at a critical disorder. These phenomena are connected to the wave nature of electrons, and can therefore be extended to any type of waves propagating in a disordered medium—such as electromagnetic waves—as proposed by Anderson [3]. Despite a significant experimental effort, studies claiming to have observed AL of light in 3D systems have all failed due to various experimental artifacts [4]. In recent years, numerous theoretical and numerical studies have led to significant progress towards a better understanding of AL of light [5–8]. Maxwell equations' specific nature is theoretically invoked to explain the challenge of localizing light in 3D systems. In 2D, it has been numerically shown that scalar electromagnetic waves were easier to localize than vector waves [9]. Additionally, correlations in the disorder are recognized to facilitate it [10].

It is worth noting that localization of light does not require disorder. For example, it has been observed in periodic photonic lattices exhibiting a flat band [11,12], or in photonic moiré superlattices [13]. Recently, it has been shown that deterministic planar arrays of point dipoles arranged in Vogel spirals support long lived, localized modes in 3D using the full vector field [14], even though the geometrical support of the array is bidimensional. In addition to localization of vectorial waves, Vogel spirals have been shown to exhibit unique electromagnetic properties that cannot be found in disordered, periodic, and quasiperiodic structures [15–18]. The observed localization of electromagnetic waves in completely deterministic Vogel spirals is different from Anderson localization where uncorrelated disorder is a key ingredient. However,

#514886
Journal © 2024
https://doi.org/10.1364/OME.514886
Received 1 Dec 2023; revised 22 Jan 2024; accepted 23 Jan 2024; published 29 Feb 2024

light localization in Vogel spirals has characteristics in common with Anderson localization in uncorrelated disorered 3D systems as the scaling behavior of the Thouless conductance and level spacing statistics [14].

In this paper, using a microwave setup and dielectric cylindrical scatterers, we show experimentally that aperiodic Vogel spirals localize much more efficiently electromagnetic waves than disordered structures when the field is not confined in 2D. The paper is organized as follows: In § 2, we introduce the experimental setup and the data extraction procedure to retrieve the individual modes. In § 3, we show that the Vogel spirals display two full bandgaps, in contrary to disordered systems. We will look for localized modes in the vicinity of these bandgaps. Finally, in § 4, we show how the change in dimension affects the localization properties in Vogel spirals and in disordered systems.

The structure of the paper allows for a full and comprehensive description of the experimental details, such as data acquisition and processing stages, which have been used to observe electromagnetic localization in Vogel spirals. By providing an experimental roadmap to describe microwave transport in Vogel spirals reported in [19], we demonstrate that the latter can outperform uncorrelated disordered systems to achieve electromagnetic localization in higher dimensions. Indeed, we show how the dimensionality of the system can be controlled in the experimental setup, enabling us to demonstrate that the electromagnetic modes supported by Vogel spirals are robust against the 2D to 3D crossover. By doing so we introduce and describe a novel system platform to demonstrate electromagnetic localization in 3D, which has never been experimentally observed with uncorrelated disordered dielectric systems so far, yet recently predicted numerically in metallic systems [8].

2. Setup and data extraction

2.1. Microwave setup

We investigate two different lattice structures, both comprised of N identical dielectric cylinders made of TiZrNbZnO ceramics (from Exxelia Temex manufacturer), with a dielectric permittivity of $\varepsilon \approx 45$ (refractive index $n \approx 7$), a radius of 3 mm and a height of 5 mm. One type of lattice features aperiodicity, as the cylinders are arranged in a Vogel spiral. The second type exhibits positional disorder.

Positions in a Vogel spiral array are defined in terms of polar coordinates (r, θ) as

$$\begin{aligned} r_i &= a_0\sqrt{i}, \\ \theta_i &= i\alpha, \end{aligned} \tag{1}$$

where $i = 1, 2, \ldots$ is an integer, the *scaling factor* a_0 is a positive constant that sets the particle separation, and the *divergence angle* α determines the constant aperture between successive points. One of the possible definitions of the angle α is as a function of an irrational number ξ, as $\alpha = 2\pi\,[1 - \mathrm{frac}(\xi)]$ where $\mathrm{frac}(\xi)$ is the fractional part of ξ. With $\alpha/(2\pi)$ irrational, Vogel spirals are characterized by the absence of rotational and translational symmetries. Here, we study the *Golden-Angle* (GA) Vogel spiral, also known as "sunflower spiral" which is obtained when ξ equals the golden number: $\xi = (1 + \sqrt{5})/2$, resulting in $\alpha \approx 2.4$ (137.508°), also known as the "golden angle". Experimentally, we implement a GA spiral made up by $N = 390$ cylinders, and a scaling factor $a_0 = 6.93$ mm, leading to a radius $R_0 = 140$ mm with a planar two dimensional (2D) density $\rho \approx 0.65$ cm^{-2}. The sketch of the GA spiral map used to place the cylinders is shown in Fig. 1(a).

The disordered array (DS) is composed by placing N hard disks according to the algorithm developed in [20]. We chose hard disks correlations as they are easily implemented in our setup: the resulting point patterns automatically fulfill the fact that the dielectric cylinders can not overlap. On the other hand, it has been shown that the precise type of disorder does not influence

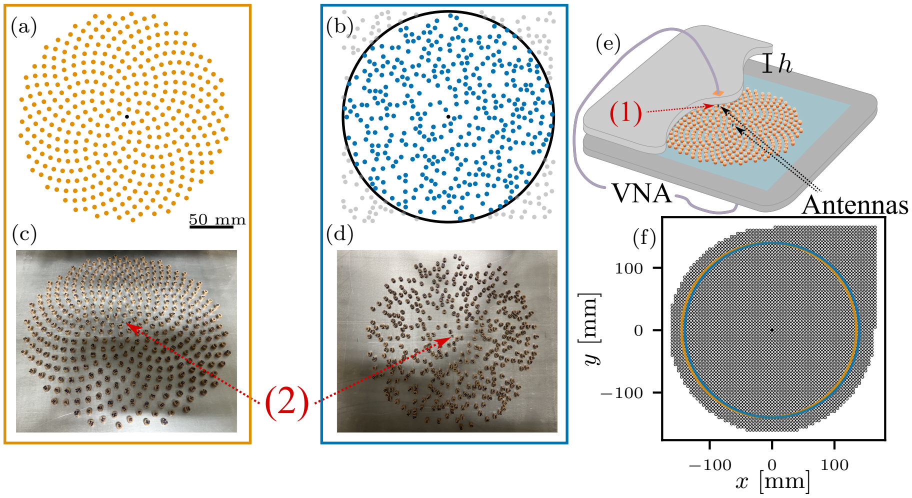

Fig. 1. (a) Golden-angle spiral array consisting of $N = 390$ cylinder created with $a_0 = 6.93$ mm and $\xi = (1 + \sqrt{5})/2$. (b) Disordered array consisting of $N = 497$ hard disks created by the software in [20] with $\phi = 0.2199$ (blue and gray dots). The circle of radius 140 mm encloses $N = 388$ sites (blue dots). In both (a) and (b), the black dot indicates the position of the fixed antenna (2), which determines the origin of the reference system. (c) Image of the 2D GA spiral array of dielectric cylinders. (d) Image of the 2D disordered array of dielectric cylinders. In both (c) and (d), the top plate has been removed to reveal the details of the sample. (e) Typical configuration of the experimental microwave setup. Cylinders are placed between two parallel aluminum plates separated by a distance h>5 mm. A vector network analyzer measures the complex signal of transmission between the fixed antenna (2), placed at the center of a fixed aluminum bottom plate, and the antenna (1), positioned at the center of the movable top plate. (f) The experimental map used to scan the cavity (gray dots). Golden (blue) circle delineates the GA spiral (DS lattice).

much the bandgap and localization properties [20]. The code is basically an isochoric Monte Carlo simulation of hard disks of radius R in a square surface of area A with periodic boundary conditions. At a given time, the center positions of the N disks generate a pattern of points, with a packing density $\phi = N\pi R^2/A$. To get the disordered array, an initial random configuration is compressed up to the target density and then relaxed to reach equilibrium. As mentioned in [20], an equilibration time set at 10^4 Monte Carlo sweeps is sufficient to equilibrate the sample. The lattice used in our experiments consists of $N = 497$ disks of radius $R = 3.25$ mm confined in a squared box of side 140 mm, leading to the packing density $\phi = 0.2199$ and to the same 2D density than the GA spiral $\rho \approx 0.65$ cm^{-2}. For comparison with the GA spiral, only sites enclosed within a circular area of radius 140 mm are selected, resulting in a disordered lattice of $N = 388$ sites as shown in Fig. 1(b).

Dielectric materials are precisely (±0.1 mm) positioned on the bottom plate of a metallic cavity using a motorized XY-stage (Newport IMS600C). Images of the GA and DS lattices are shown in Fig. 1(c) and (d), respectively. The cavity is made of two parallel aluminum plates separated by a distance h>5 mm. The bottom plate is covered by a self-adhesive thin plastic film assuring uniform electrical contact with the cylinders, thus improving reproducibility [see Fig. 1(e)]. The electric field in the cavity is induced and measured by two straight antennas placed at the center (1) of the movable top plate and (2) of the bottom plate, the antenna (2) also defines the origin of the reference system $(x, y) = (0, 0)$. As the two antennas are linear and perpendicular to the plane of the cavity, they excite only the z-component E_z of the electric field $\vec{E}$, thus imposing transverse magnetic (TM) polarization in a 2D cavity. For this polarization, cylinders act as Mie scatterers on the electromagnetic field [21,22]. We refer the reader to Fig. 1 in the Sup. Mat. of Ref. [23] where the scattering efficiency of an individual cylinder is presented in the pure 2D limit ($h = 5$ mm). Under this polarization, the electromagnetic field can be reduced to a scalar field below the cutoff frequency $\nu_{\text{cut}} = c_0/(2h)$, where c_0 is the speed of light in air, because only the fundamental TM_0 mode can propagate [$E_z(x, y)$ does not depend on z] and the empty cavity can be completely considered as 2D. Our experiments are carried out considering three different values of h (13 mm, 15 mm and 17 mm) in the frequency range [5.5 GHz, 15 GHz], corresponding to wavelengths in the range [55 mm, 20 mm]. It is worth noting that the cavity cannot be viewed as purely 2D over the whole range, a transition to a three-dimensional regime occurs: the higher the cavity height, the lower the transition frequency.

Using the movable antenna (1), a 160 mm radius disk centered on the origin is mapped using a 5×5 mm^2 square grid. Additionally, the electric field outside the lattice is measured on sites belonging to the upper right corner of a 165 mm size square enclosing the disk [see Fig. 1(f)]. The final measured map contains 3675 points and is shown in Fig. 1(f), where the golden [blue] circle delineates the GA spiral [DS lattice], whose geometrical center is located at $(x, y) = (-5 \text{ mm}, 0)$ [$(x, y) = (0, 0)$], and grey points represents the measured positions. At each position (x, y), both complex reflected and transmitted signals are registered ($S_{11}(\nu)$ and $S_{21}(\nu)$, respectively) using a Vector Network Analyser (VNA, ZVA 24 from Rohde & Schwarz). Examples of the intensity of both measured signals, $|S_{11}|^2$ (purple line) and $|S_{11}|^2$ (orange line), are presented in Fig. 2(a) and (b) for the GA spiral and the DS lattice, respectively. Both panels show measurements taken at a given distance $d \approx 106$ mm between the antennas for a distance between plates $h = 13$ mm. The weak coupling regime between the antenna and the field explains the low transmission values observed in both panels. In Fig. 2(a), frequency regions with values of the reflection close to 1 and vanishing transmission values indicate the presence of bandgaps. Particularly, two frequency windows with these characteristics are identified around ~ 9 GHz and ~ 11 GHz for the GA spiral case. In comparison, a unique and smaller frequency range with low transmission and high reflection is observed for the DS array around ~ 9 GHz [see Fig. 2(b)]. A posterior analysis of the transmitted signal is conducted using the harmonic inversion method, as described thoroughly in the following section.

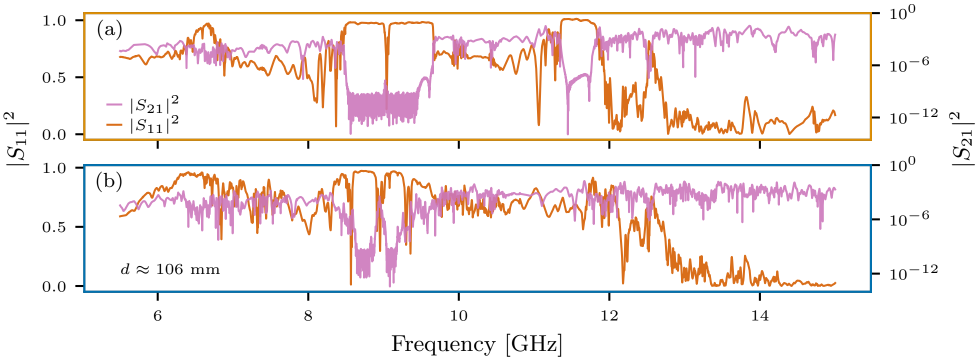

Fig. 2. Reflected $|S_{11}(\nu)|^2$ (orange line) and transmitted coefficients $|S_{12}(\nu)|^2$ (purple line) for (a) the GA spiral and (b) the DS lattice at a distance $d \simeq 106$ mm from the origin ($x = 75$mm, $y = 75$mm) in a cavity with $h = 13$ mm.

2.2. Finding the resonances of the system

According to the Breit-Wigner decomposition of the S-matrix [24], the transmission and reflection signals can be viewed as the superposition of complex resonances, each of which being represented by a Lorentzian function, i.e., by four parameters: the frequency ν_k, the width $\delta\nu_k$, and the complex amplitude A_k. Due to the specific use we will make of it, we will concentrate here only on the complex resonance sum decomposition of the transmission signal. The latter can be written for any given measurement position as

$$S_{21}(\nu) = \sum_k \frac{A_k}{\nu - \nu_k + \mathrm{i}\delta\nu_k}, \tag{2}$$

where the sum runs over all resonances.

Given the huge amount of unknown parameters, the extraction of the resonances from the raw signal is not a trivial task. Here, we use a powerful tool known as *harmonic inversion* to obtain all the resonances parameters of a complex signal. This method was firstly introduced by Wall and Neuhauser [25], and then improved by Mandelshtanm and Taylor [26,27]. To apply the harmonic inversion to our experimental signals, we start by choosing a frequency filter $g(\nu)$ defined as

$$g(\nu) = \begin{cases} 1 \quad \text{for} \quad \nu \in [\nu_0 - \Delta\nu, \nu_0 + \Delta\nu], \\ 0 \qquad\quad \text{everywhere else,} \end{cases} \tag{3}$$

where the spectrum (2) is expected to have just $K \sim 50 - 200$ resonances inside the interval $[\nu_0 - \Delta\nu, \nu_0 + \Delta\nu]$. Then, the filtered spectrum $S'_{12}(\nu) = f(\nu) \times g(\nu) = \sum_{k=1}^{K} \frac{A_k}{\nu - \nu_k + \mathrm{i}\delta\nu_k}$ is Fourier transformed to the time domain to obtain a band-limited signal

$$C(t) = \frac{1}{2\pi} \int_{\nu_0 - \Delta\nu}^{\nu_0 + \Delta\nu} S'_{12}(\nu) \mathrm{e}^{-\mathrm{i}(\nu - \nu_0)t} \mathrm{d}\nu = \mathrm{i} \sum_{k=1}^{K} A_k \mathrm{e}^{-\mathrm{i}(\omega_k - \nu_0)t}, \tag{4}$$

with the complex resonance frequency $\omega_k = \nu_k - \mathrm{i}\delta\nu_k$, and $\nu_k \in [\nu_0 - \Delta\nu, \nu_0 + \Delta\nu]$. Additionally, the introduction of ν_0 into the exponential shifts the signal by $-\nu_0$ in the frequency domain and relocates it around 0, decreasing the phase oscillations of the band-limited signal $C(t)$. Finally, Eq. (4) can be discretized in a $2K$ equidistant grid with time step $\tau = \pi/\Delta\nu$

$$c_j = C(t = j\tau) = \mathrm{i} \sum_{k=1}^{K} A_k \mathrm{e}^{-\mathrm{i}(\omega_k - \nu_0)j\tau}, \qquad j \in [\![0, 2K - 1]\!], \tag{5}$$

reducing the problem of finding the resonances to the resolution of a set of $2K$ nonlinear equations

$$c_j = \mathrm{i} \sum_{k=1}^{K} A_k z_k^j, \qquad j \in [\![0, 2K - 1]\!], \tag{6}$$

where $z_k = \mathrm{e}^{-\mathrm{i}(\omega_k - \nu_0)\tau}$.

The strategy to solve Eq. (6) is to convert the system of nonlinear equations into a linear algebra problem. We start by expressing K of its elements in a matrix representation

$$\begin{pmatrix} c_{j+1} \\ \vdots \\ c_{j+K} \end{pmatrix} = \mathrm{i} \begin{pmatrix} z_1^{j+1} & \dots & z_K^{j+1} \\ \vdots & & \vdots \\ z_1^{j+K} & \dots & z_K^{j+K} \end{pmatrix} \begin{pmatrix} A_1 \\ \vdots \\ A_K \end{pmatrix} \longrightarrow \begin{pmatrix} z_1^{j+1} & \dots & z_K^{j+1} \\ \vdots & & \vdots \\ z_1^{j+K} & \dots & z_K^{j+K} \end{pmatrix}^{-1} \begin{pmatrix} c_{j+1} \\ \vdots \\ c_{j+K} \end{pmatrix} = \mathrm{i} \begin{pmatrix} A_1 \\ \vdots \\ A_K \end{pmatrix}, \tag{7}$$

then, we replace Eq. (7) into Eq. (6) to get

$$c_j = \begin{pmatrix} z_1^j \dots z_K^j \end{pmatrix} \begin{pmatrix} z_1^{j+1} & \dots & z_K^{j+1} \\ \vdots & & \vdots \\ z_1^{j+K} & \dots & z_K^{j+K} \end{pmatrix}^{-1} \begin{pmatrix} c_{j+1} \\ \vdots \\ c_{j+K} \end{pmatrix} = \sum_{k=1}^{K} a_k c_{j+k}, \tag{8}$$

where, we observe that every signal point c_j can be computed from a linear combination of the next K points, and is determined by the coefficients a_k with $k = 1, \ldots, K$. Now, by substituting Eq. (6) into both sides of Eq. (8), we obtain

$$\mathrm{i}\sum_{k=1}^{K} A_k z_k^j = \mathrm{i}\sum_{k=1}^{K}\sum_{l=1}^{K} a_l A_k z_k^{j+l} \longrightarrow \sum_{k=1}^{K}\left[\sum_{l=1}^{K} a_l z_k^{j+l} - z_k^j\right] A_k = 0, \tag{9}$$

which is satisfied for an arbitrary set of amplitudes A_k. Thus, the values $z_k = \mathrm{e}^{-\mathrm{i}(\omega_k - \nu_0)\tau}$ are given as the zeros of the polynomial

$$\sum_{l=0}^{K} a_l z^l = 0 \quad \text{with} \quad a_0 = 1, \tag{10}$$

and finding them represents the only nonlinear step of the method. The roots of a polynomial can be found by the diagonalization of the Hessenberg matrix

$$\mathbf{A} = \begin{pmatrix} -\frac{a_{K-1}}{a_K} & -\frac{a_{K-2}}{a_K} & \ldots & -\frac{a_1}{a_K} & -\frac{a_0}{a_K} \\ 1 & 0 & \ldots & 0 & 0 \\ 0 & 1 & \ldots & 0 & 0 \\ \vdots & \vdots & & \vdots & \vdots \\ 0 & 0 & \ldots & 1 & 0 \end{pmatrix}, \tag{11}$$

which is highly robust for finding the zeros of a high degree polynomial. As a last step, the values of z_k are substituted in Eq. (6) to compute the values of the amplitude A_k.

To summarize, the four parameters of each of the resonances that make up the signal are given by (*i*) the solutions of the set of linear Eqs. (8), for a_k; (*ii*) the diagonalization of the matrix (11), for the complex frequency $\omega_k = \nu_0 + \frac{\mathrm{i}}{\tau}\ln z_k$; (*iii*) the solution of the non linear system of Eqs. (6), for the amplitude A_k.

To apply the harmonic inversion to our experimental data, the complex spectrum at each position is first divided into 19 frequency intervals, each one with a bandwidth of 0.6 GHz, overlapping each other by 0.05 GHz to avoid the interval of interest of being spoiled by spurious resonances generated by the filtering of the signal. Figure 3(a) shows the intensity of the transmitted signal $|S_{21}|^2$ at a distance $d \approx 106$ mm [($x = -75$mm, $y = -75$mm)] between antennas in the GA spiral and vertical dash-dotted lines indicate the limits of one of the chosen windows (7.95 GHz to 8.55 GHz). The complex nature of the signal is presented in Fig. 3(b), and (c) (purple lines) by means of the amplitude $|S_{21}|$ and phase $\arg(S_{21})$; or in Fig. 3(d), and (e) by the real $\mathrm{Re}(S_{21})$, and imaginary parts $\mathrm{Im}(S_{21})$ of the filtered signal shown in Fig. 3(a). As expected up to this point, no guess about the resonances that compose the signal can be done from the raw measurement. During the harmonic inversion method, the complex spectrum is Fourier transformed to obtain the band-limited signal whose intensity is shown in Fig. 3(f). $|C(j\tau)|$ is characterized by sharp peaks for small values of j up to certain limit ($j \sim 250$ in this case). Such peaks disappear and the signal falls below the level of noise. We use twice the value of this transition to set the value of $2K$ needed in Eq. (5). Note that this value is different for each studied interval. In this example, the harmonic inversion algorithm was fed with the value $2K = 500$ [dashed line in Fig. 3(f)]. The choice of K sets exactly the number of resonances that will be found by the algorithm.

To ensure the robustness of the result, three different criteria are used to discriminate spurious resonances recovered by the harmonic inversion. As a first criterion, the non linear system (6) is

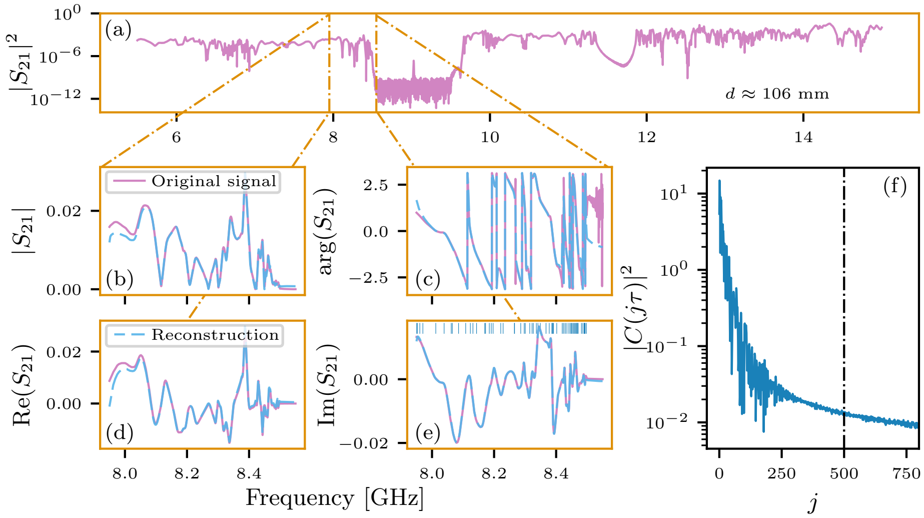

Fig. 3. (a) Transmitted intensity $|S_{12}(\nu)|^2$ for the GA spiral at a given distance $d = \sqrt{x^2 + y^2}$ ($x = -75$mm, $y = -75$mm) from the origin of the reference system. Golden dash-dotted lines indicate the frequency interval considered in this example (7.95 GHz $\leq \nu \leq$ 8.55 GHz). (b) Amplitude $|S_{12}(\nu)|$, (c) phase $\arg(S_{12}(\nu))$, (d) real part $\mathrm{Re}(S_{12}(\nu))$ and (e) imaginary part $\mathrm{Im}(S_{12}(\nu))$ of the complex filtered signal shown in (a). Purple continuous line represent the original signal while indigo dashed lines are Eq. (2) evaluated for the resonances obtained by the harmonic inversion. Blue vertical lines in (e) display the frequencies $\Re P\omega_k$ recovered by the harmonic inversion method. (f) Intensity of the band-limited signal $|C(j\tau)|^2$ corresponding to the Fourier transform of the filtered signal shown in (b), (c), (d) and (e). The black dash-dotted line indicates the value $2K = 500$ considered in this example.

solved twice, once by considering $j = 0, \ldots, 2K - 1$ and, then with $j = 1, \ldots, 2K$. Later, both results are compared, and the resonances depending on the choice of j or out of the limits of the filter, are discarded. The second discrimination is carried on by considering that all resonances whose amplitude $|A_k|<10^{-8}$ GHz are the result of the noise in the original signal, and are also discarded. Finally, only resonances with sufficient resonance depth/height are taken into account. To do this, we compare the amplitude A_k versus the width of the resonance given by $\delta\nu_k$ of the resonance. Numerically we choose $|A_k|/\delta\nu_k>10^{-4}$. The result of the harmonic inversion after filtering with the three discriminating criteria is shown in in Fig. 3(b), (c), (d), and (e), where a reconstruction of the corresponding complex signal is represented by the dashed indigo line. A good agreement between the original signal and its reconstruction is observed. In this case, a total of 61 resonances were found in this interval, and their absolute frequencies $\Re P\omega_k$ are plotted in Fig. 3(e) where each vertical blue line represents a resonance.

2.3. Recovering the spatial distribution of an eigenstate

Once we are able to find the parameters of the resonances that compose one complex signal, the process can be repeated over all the measured spatial positions shown in Fig. 1(f). Each resonance k extracted using the HI procedure is therefore associated with a position on the map (x_k, y_k) and can then be represented in a 6-dimensional space. An example of the resulting data is shown in Fig. 4 for the GA spiral, where resonance density maps (from dark blue to yellow) are depicted. In Fig. 4, the spatial positions (a) x_k and (b) y_k as well as (c) the phases $\arg(A_k)$, (d) the widths $\delta\nu_k$ and (e) the amplitudes $|A_k|$ of each resonance extracted by the harmonic inversion are plotted as a function of the frequencies ν_k in a short frequency window (8.42 GHz $\leq \nu_k \leq$ 8.52 GHz).

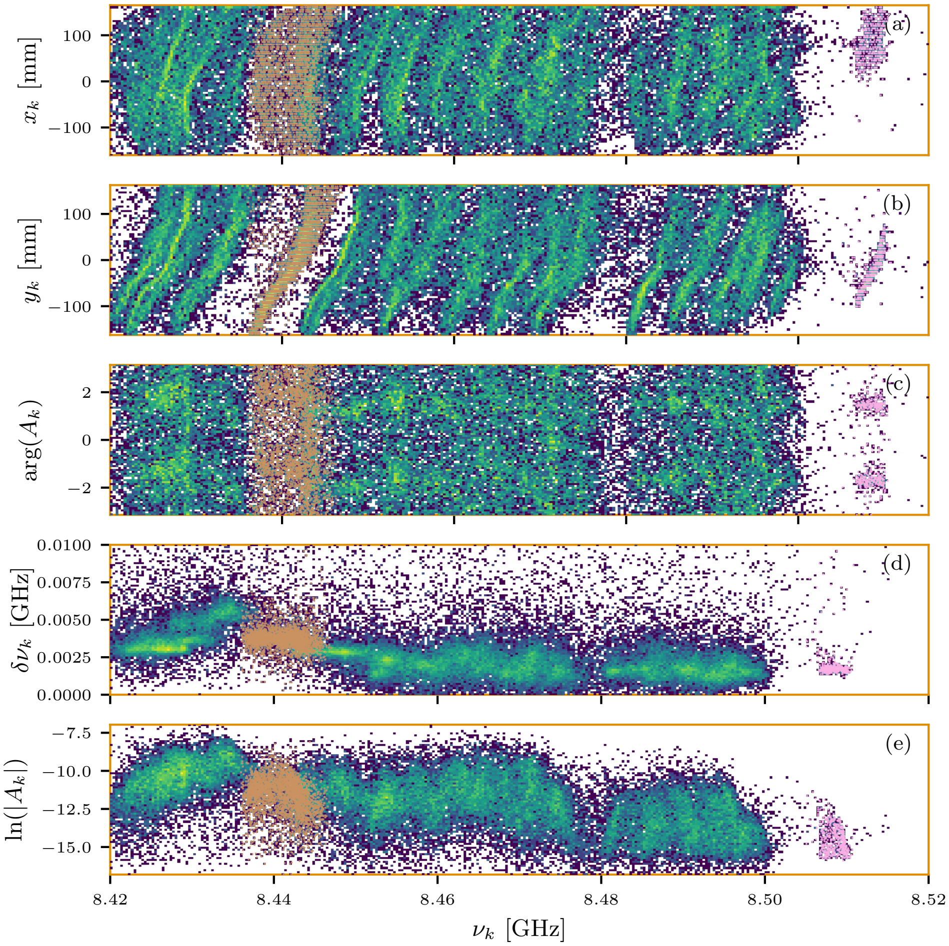

Fig. 4. Spatial positions (a) x_k and (b) y_k, (c) phases $\arg(A_k)$, (d) widths $\delta\nu_k$ and (e) logarithm of the amplitudes $|A_k|$ as a function of the frequencies ν_k extracted by the harmonic inversion for the GA spiral. Density plots allows the identification of modes (regions with high-density of resonances). Brown and pink dots show two different examples of clusters.

As a result of the high point density in certain regions, different structures made up of clusters emerge. Such clusters are directly related with the eigenmodes of the system and their correct identification and delimitation was previously used to find the number of states carried by the system [23] [which is proportional to the density of states (DoS) introduced below].

All resonances belonging to the same cluster should ideally possess the same frequency. Due to the presence of the measurement antenna, the resonance frequencies extracted at a given spatial position are affected differently and slightly shifted according to the electromagnetic field intensity at that point [28]. By allowing the mobile antenna to penetrate only slightly into the cavity, in practice 3 mm, this effect is reduced, but still present [24]. Additionally to the presence of the antenna, small local variations in the cavity height also modify the resonance frequencies. To reduce this effect, the distance between plates is measured at different positions ensuring a variation <1 mm. The combination of these two effects explains the dispersion of the Lorentzian parameter values observed in Fig. 4.

For the identification of all data points belonging to a certain cluster [see e.g. Figure 4], a density-based algorithm [29] is implemented. Specifically, we use in a slightly modified version of the C-DBSCAN algorithm [23], firstly proposed by Ruiz, *et al.* [29]. C-DBSCAN identifies point neighbourhoods in a d-dimensional metric space and requires no a priori knowledge of the shape, number of points or data distribution of the cluster. In our case, the metric space can be freely chosen as (x, y, ν), $(x, y, \nu, \delta\nu)$, $(x, y, \nu, \ln|A|)$, or $(x, y, \nu, \delta\nu, \ln|A|)$ in order to obtain the best clustering results at the desired frequency. In addition, each cluster must satisfy the constraint of not containing two points with the same (x, y) coordinates. The procedure is highly efficient, but cannot be fully automated. The main difficulties are of two kinds: (*i*) when the amplitude of the resonances is of the order of the noise, the harmonic inversion procedure fails; (*ii*) when two or more clusters interpenetrate too densely, preventing their identification.

After selecting a given cluster [see, e.g., brown dots in Fig. 5(a) for the DS], a phase rotation is applied on the complex amplitudes $D_k = \mathrm{e}^{\mathrm{i}\alpha} A_k$ such that their real and imaginary parts become independent variables [30]

$$\tan 2\alpha = -\frac{2\langle \mathrm{Re}(A_k)\mathrm{Im}(A_k)\rangle}{\langle \mathrm{Re}(A_k)\rangle^2 - \langle \mathrm{Im}(A_k)\rangle^2}. \tag{12}$$

Figure 5(b) illustrates the effect of rotation in the complex plane when applying Eq. (12). The existence of a phase reference allows to represent the complex mode through its signed amplitude:

$$E_k = |D_k| \mathrm{sgn}\left[\mathrm{Re}\left(D_k\right)\right] . \tag{13}$$

The spatial modal structure (Eq. (13)) of the cluster shown in Fig. 5(a) and (b) is reconstructed in Fig. 5(c).

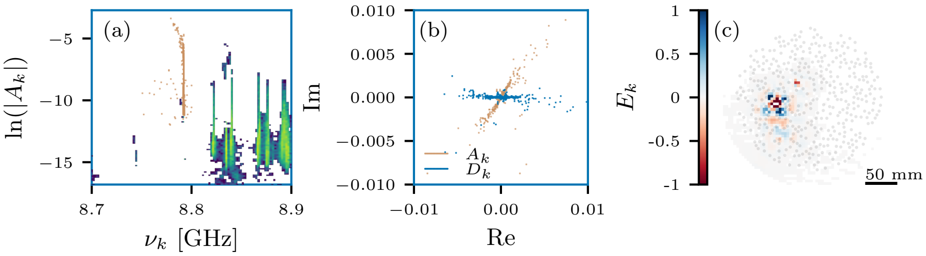

Fig. 5. (a) Density plot of the amplitudes $|A_k|$ as a function of the frequencies ν_k, extracted via the harmonic inversion for the DS lattice. Brown dots represent one selected cluster. (b) Real and imaginary parts of the complex amplitudes A_k (brown dots) and D_k (blue dots). The amplitude A_k is directly extracted from (a) while D_k is its corresponding phase rotated amplitude. (c) The spatial modal structure of the cluster shown in (a) after the rotation.

3. Formation of bandgaps in spirals

3.1. Density of states

As the harmonic inversion technique is unable to extract all the resonances within the entire frequency domain, we have to cope with an incomplete set of resonances and thus cannot build correctly the density of states. Yet this quantity is of crucial interest to identify different transport regimes [19]. Fortunately, due to its connection with the singularities of the Green's function [31], the Local Density of States (LDoS) is directly related to the real part of the reflection term of the scattering matrix (see Appendix A of [32]). In the regime of weakly coupled antennas, an excellent approximation of the LDoS is given by $\mathrm{LDoS}(\vec{r}) = 1 - |S_{11}|^2$, where antenna (1) is positioned at $\vec{r}$. The advantage of using the absolute value instead of the real part is that the raw experimental reflection spectra have a global frequency-dependent phase factor, which requires an additional experimental step to eliminate [33]. Since the error is second-order in the weak coupling parameter, we will use the latter LDoS expression in the following. Consequently, up to an inversion, oranges curves in Figs. 2 can be reinterpreted as the LDoS at different positions for the two lattices. It is worth noting that the LDoS reconstruction via the scattering matrix does not rely on the perfect knowledge of all individual resonances.

Straightforwardly, the density of states (DoS) can be obtained by averaging the LDoS over all measured positions

$$\mathrm{DoS} = \langle \mathrm{LDoS} \rangle_{\text{all positions}} = 1 - \langle |S_{11}|^2 \rangle_{\text{all positions}}. \tag{14}$$

In Fig. 6, the DoS corresponding to (a) the GA spiral and (b) the DS lattice in a cavity with height $h = 13$ mm are plotted as a function of the frequency, both curves being computed according to Eq. (14). Additionally vertical dash-dotted black lines are added to indicate the 2D threshold in the empty cavity $\nu_{\mathrm{cut}}(h = 13\text{ mm}) \approx 11.52$ GHz. An increment in the number of states supported by the structures is recognized above the cutoff frequency in both cases. Nevertheless, the GA spiral presents two long flat valleys, identified as bandgaps, which are highlighted by two grey stripes in Fig. 6(a). The peaks inside the first gap are a signature of the lattice's defect modes, which are caused by slight scatterers imperfections. In contrary to the GA spiral case, the DoS of the DS lattice does not present any clear bandgap [Fig. 6(b)]. However a reduction in the number of states is still visible in the frequency region where the GA spiral possesses its first gap, while the second bandgap has completely disappeared. Instead of the narrow defect peaks observed in the GA spiral at approximately 9.1 GHz, this case displays a distributed set of small peaks throughout the region between 8.5 GHz and 9.7 GHz.

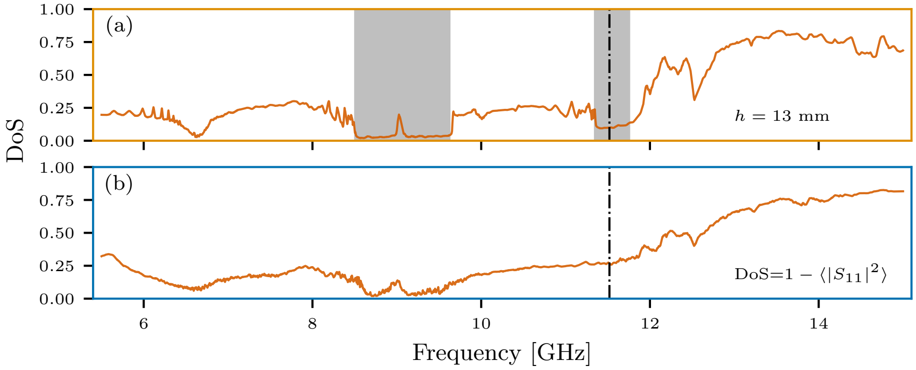

Fig. 6. Experimental density of states (DoS) computed from Eq. (6) for both (a) the GA spiral and (b) the DS in a cavity with $h = 13$ mm. Frequency windows identified as bandgaps are highlighted (grey stripes). Dash-dotted black vertical lines mark the 2D frequency limit $\nu_{\mathrm{cut}} \approx 11.52$ GHz.

3.2. Spiral defect modes extraction

We now focus on the first bandgap to study the defect modes of the GA spiral system. As explained above, the amplitude of the electric field of an eigenmode can be recovered thanks to harmonic inversion and the clustering methods. Figures 7(a) and (b) show the reconstruction of the amplitude of two localized defect modes with frequencies $\nu_k \approx 9.2$ GHz. Such modes are characterized by the fact that they are supported by a small quantity of cylinders (<10), and, in contrary to the states previously studied in those structures [19], they are not centered at the center of the spiral. Thus, the radial decay of the mode amplitudes is not easy to determine unambiguously. In this case, the most suitable quantity for correctly studying the decay law of these modes is given by the spatial autocorrelation (SA) [34], with the property of being centered at the origin. In 2D, the SA function is defined as

$$\mathrm{Cor}(E_k)(x',y') = \int_{-\infty}^{\infty}\int_{-\infty}^{\infty} E_k^*(x,y)E_k(x+x',y+y')\mathrm{d}x\mathrm{d}y. \tag{15}$$

where the Wiener-Khinchin theorem allows to reinterpret Eq. (15) in terms of the Fourier transform of the complex amplitude E_k as

$$\mathrm{Cor}(E_k)(x',y') = \left|\mathcal{F}^{-1}\left\{|\mathcal{F}\left\{E_k(x,y)\right\}|^2\right\}\right|. \tag{16}$$

The evaluations of Eq. (16) for the defect states shown in Figs. 7(a) and (b) are depicted on Figs. 7(c) and (d), respectively. The radial decay of the SA is computed by angular averaging around the well-defined origin. The corresponding radial decays are plotted in Figs. 7(e) and (f), showing an exponential law in both cases. Here $r' = \sqrt{x'^2 + y'^2}$ is the radial coordinate of the autocorrelation space with (x', y') the corresponding Cartesian coordinates. Additionally, in the particular case of an exponential function, Eq. (16) allows us to prove that

$$\mathrm{Cor}(E_k) \propto \mathrm{e}^{-r'/\xi_{\mathrm{lkoc}}}, \tag{17}$$

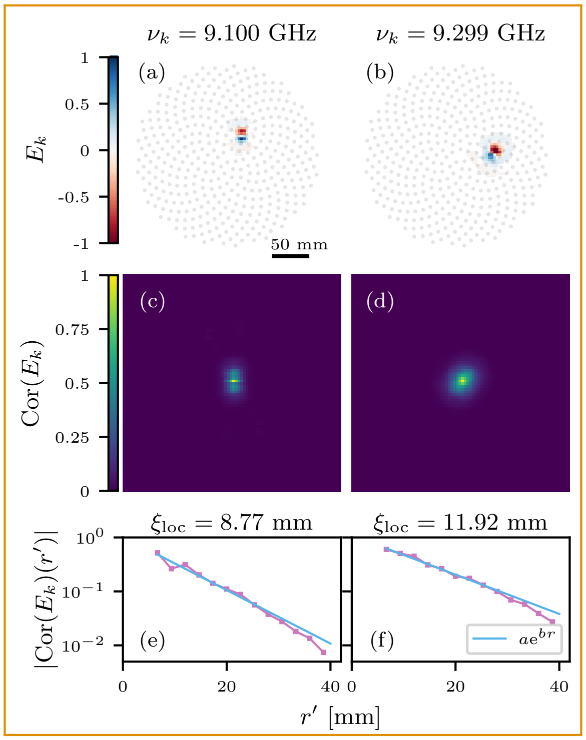

Fig. 7. (a) [(b)] Spatial modal structure, (c) [(d)] spatial autocorrelation field, and (e) [(f)] radial profile of the spatial autocorrelation field of a representative defect eigenmode in the GA spiral with $h = 13$ mm. Amplitude maps are normalized such that $\max(|E_k|) = 1$, thus $\max(|\mathrm{Cor}(E_k)|) = 1$. Both modal structures are just supported by a few dielectric cylinders and present a spatial extension similar to their spatial autocorrelation. Radial decays (pink dots) are obtained by performing an angular average in the autocorrelation space (r' is measured from the well defined autocorrelation center).

where ξ_{loc} is the localization length which can thus be extracted from the experimental data. This quantity indicates the spatial extension of an exponentially localized mode allowing to define a criterion to determine if the states are ($\xi_{\text{loc}} \lessapprox R_0$) or not ($\xi_{\text{loc}} > R_0$) confined inside the structure.

4. Dimensional robustness of the modes

In the previous section, we have shown how all resonance parameters are extracted from the original signal via the harmonic inversion method. Then, by identifying the points belonging to the same cluster, we can determine the characteristics of each individual mode. Besides the local mode analysis, we also presented how the DoS can be directly computed from the measured reflected signal, providing an overview of the characteristics of different frequency regions. We now use the results of harmonic inversion, together with the DoS, to unravel the global consequences of the 2D/3D transition, achieved by changing the distance between the top and bottom plates. The local frequency behavior is then studied via the eigenmodes of the system. We start by computing the quality factor $Q_k = \nu_k/\delta\nu_k$ for all resonances extracted by the harmonic inversion. The quality factor estimates the strength of the energy confinement in the system for a given resonance. In Figs. 8(a), (c), and (e) [(b), (d), and (f)], Q_k is plotted as a function of ν_k for the GA spiral [DS] in the cases $h = 13$ mm, $h = 15$ mm, and $h = 17$ mm, respectively. The corresponding DoS are also depicted in Figs. 8(g) [(h)].

4.1. Golden-angle spiral

We start our analysis by focusing on the GA spiral case. At low frequency (ν<8.5 GHz) and for all values of h, we observe in Figs. 8(a), (c) and (e) an increase of the quality factor Q_k of the resonances, going from values close to zero when $\nu \sim 8$ GHz, to reach a maximum at the border of the first bandgap. This is in agreement with all three DoS curves that present a similar behavior between them, being just differentiated by their intensity [Fig. 8(g)]. Since this frequency region always lies below the estimated 2D threshold, the difference in the signal intensity simply reflects the variation in the antenna coupling with the height.

Three representative states populating the bandgap edge are shown in Fig. 9(a), (b) and, (c) for $h = 13$ mm, $h = 15$ mm, and $h = 17$ mm, respectively. Figs. 9(d), (e) and (f) present the radial averages of these modes performed from the geometrical center of the spiral $(x, y) = (-5\text{ mm}, 0)$. As in Ref. [19], we test different radial decays (Gaussian, power-law, or exponential) and show the best fit discriminated by minimizing the sum of the squared residuals (Gaussian in the three cases presented here). Additionally, all three modes are characterised by huge Q_k values as expected from Fig. 8. Confined Gaussian band edge states result from Bragg scattering in the arms of the spiral given the inhomogeneity distribution of spacing between neighbouring cylinders [35]. The existence of such modes is attributed to the specific correlations of the cylinder positions in the structure and is predicted to take place for $\rho c_0^2/\nu^2 > 3.5$ (ν<12.9 GHz in our experimental spiral) [14].

As already mentioned, in the $h = 13$ mm case, the first bandgap (8.5 GHz<ν<9.7 GHz) is populated by defect states at ~ 9.1 GHz. These peaks stay unchanged when increasing the height of the cavity and are composed of states such as those observed in Fig. 7 for $h = 13$ mm, keeping similar quality factors ($Q_k \sim 1500$) for all different values of h. When increasing the height of the cavity, the upper band edge is pushed toward lower frequencies. In the $h = 17$ mm case, the second half of the bandgap almost completely vanishes. This closing of the gap as a function of the cavity height is due to the appearance of 3D states which can appear above the cutoff frequency. The cutoff frequencies plotted as black lines in Fig. 8 are calculated for an empty cavity, i.e., with an effective refractive index of $n = 1$. The presence of the high-refractive index scatterers in the cavity increases the value of the effective refractive index, and thus decreases the cutoff frequencies explaining the shift between the vertical lines and the upper band edge of the

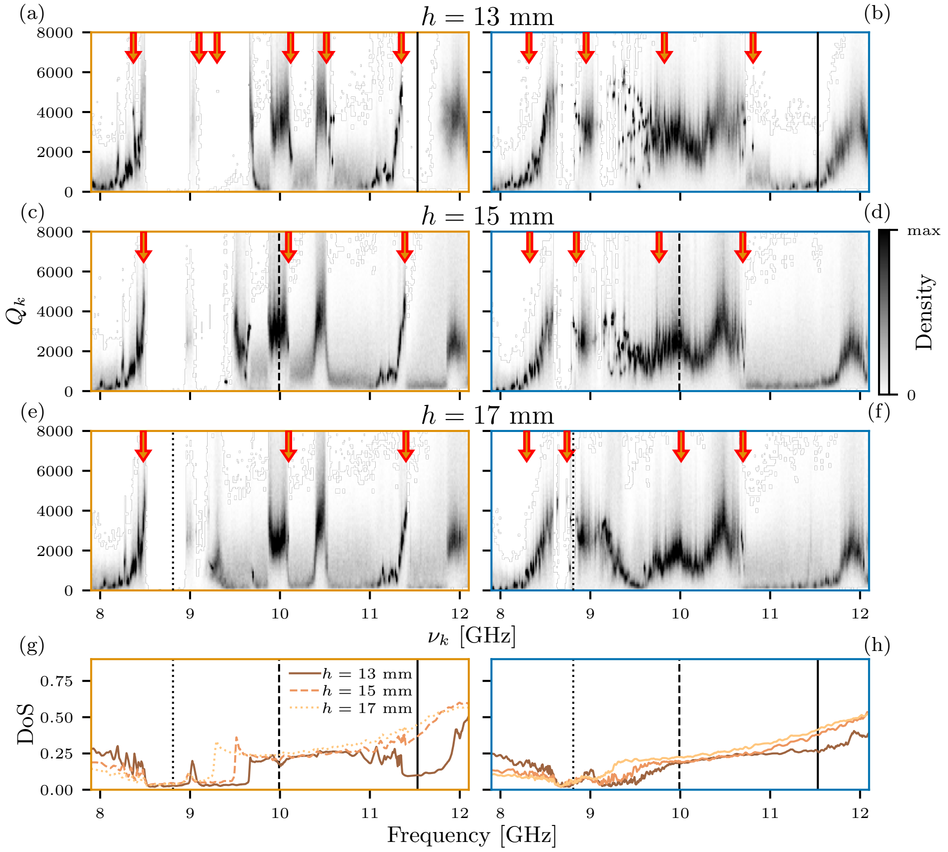

Fig. 8. Density plots of the quality factors Q_k as a function of the resonant frequencies ν_k extracted via the harmonic inversion with a distance between plates (a) [(b)] $h = 13$ mm, (c) [(d)] $h = 15$ mm, and (e) [(f)] $h = 17$ mm for the GA spiral [DS]. Arrows indicate the frequencies of the states presented in Figs. 7, 9, 10, 11, and 12. (g) [(h)] Experimental DoS for the GA spiral [DS] as a function of the frequency. Black vertical lines indicate the 3 different cut-off frequencies ν_{cut} respectively associated with the 3 heights.

first bandgap. Just above the upper band edge, the quality factors extracted from the harmonic inversion are of the same order of magnitude than the one measured for the Gaussian states found just below the lower band edge at ~ 8.5 GHz ($Q_k \sim 2000$). Unfortunately, given the high density of clusters in this region, single mode can not be clearly distinguished and separated, hindering their reconstruction with our current tools.

The first bandgap is followed by a long frequency region (9.6 GHz<ν<11 GHz) with states characterized by low quality factors ($Q_k \to 0$, apart from two bands located around 10 GHz and 10.4 GHz). Note that all DoS curves computed for the three different height keep a constant value all along this interval: The expected difference in the intensity of the signal is compensated by the new 3D emerging states. The $Q_k - \nu_k$ maps also show two stripes with higher quality factors ($Q_k \sim 2000$) located around $\nu \sim 10$ GHz and $\nu \sim 10.4$ GHz that are also robust to the dimensional change. Figures 10(a), (b) and (c) shows the spatial reconstruction of three representatives modes found at $\nu \sim 10$ GHz when $h = 13$ mm, $h = 15$ mm and $h = 17$ mm, respectively. On the other hand, at $\nu \sim 10.4$ GHz our harmonic inversion and clustering algorithms are just able to recover a few states for $h = 13$ mm [see Fig. 10(d)]. Spatial distributions of states are centered

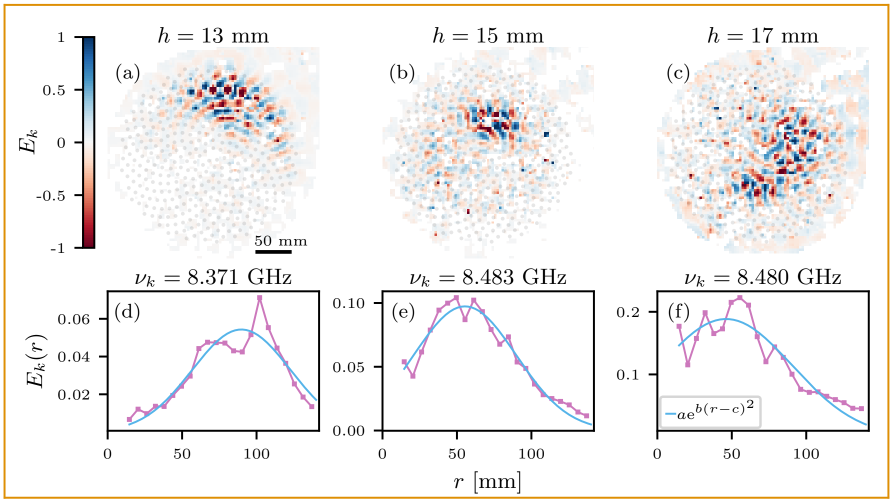

Fig. 9. [(a), (b), and (c)] Spatial modal structure and [(d), (e), and (f)] the radial profile of representative Gaussian eigenmodes. Quality factor of the modes: (a) $Q_k \approx 3931$; (b) $Q_k \approx 4375$; (c) $Q_k \approx 3586$. Amplitude maps are normalized such that $\max(|E_k|) = 1$. Radial decays (pink dots) are obtained by performing an angle averaging where $r = \sqrt{(x+5)^2 + y^2}$ is measured from the center of the spiral and expressed in mm.

around "defects", instead of the center of the spiral, but in contrary to the modes populating the first bandgap, their spatial extensions occupy the whole measured space. The analysis of the corresponding SA functions (not shown) leads to radial decay functions that are neither power-law, exponential, nor Gaussian [see Fig. 10(e), (f), and (g)]. Given the robustness of these states to the distance between plates, their insensitivity to a complete reconstruction of the spiral with the same sequence of cylinders, and their high quality factors, we think that their nature is related to the imperfections of the cylinders (in size or in dielectric permeability).

For all values of h, Fig. 8 shows that the quality factor of the resonances near $\nu \sim 11$ GHz are close to zero, illustrating a very high loss rate. On the other hand, the DoS [Fig. 8(g)] indicates the emergence of new states as the height increases. These new leaky modes which appear at frequencies much higher than the cut-off frequencies are clearly modes that exist only beyond 2D. It is therefore remarkable that the clustering analysis reveals the existence of modes whose properties are robust to the dimensional change. Three different states found in the same GA spiral in a cavity characterized by (a) $h = 13$ mm, (b) $h = 15$ mm, and (c) $h = 17$ mm are shown in Fig. 11. Notably, the mode's shape, frequency, quality factor, and radial decay function remain almost invariant and this, even beyond the 2D threshold [see Fig. 11(d), (e) and (f)]. By averaging from the center of the spiral, decay-laws are well described by Gaussian functions. These "Gaussian modes" surviving the 2D/3D transition in Vogel spirals is one of the main points reported in Ref. [19].

For $h = 13$ mm, the last studied Gaussian state has been found in the upper limit of a populated band. At higher frequency (11.5 GHz<ν<12 GHz), the presence of a second bandgap is well visible in the DoS and in the quality factors. Opening the cavity suppresses the second bandgap, which, for $h = 15$ mm and $h = 17$ mm is occupied by resonances with low quality factor ($Q_k \longrightarrow 0$) that are attributed to the 3D nature of the system. Finally, in the frequency region where the three systems are 3D (ν>12 GHz), resonances with $Q_k \sim 2000$ are recovered by the harmonic inversion. Unfortunately, in these 3D situations, the large modal overlap regime (mean mode

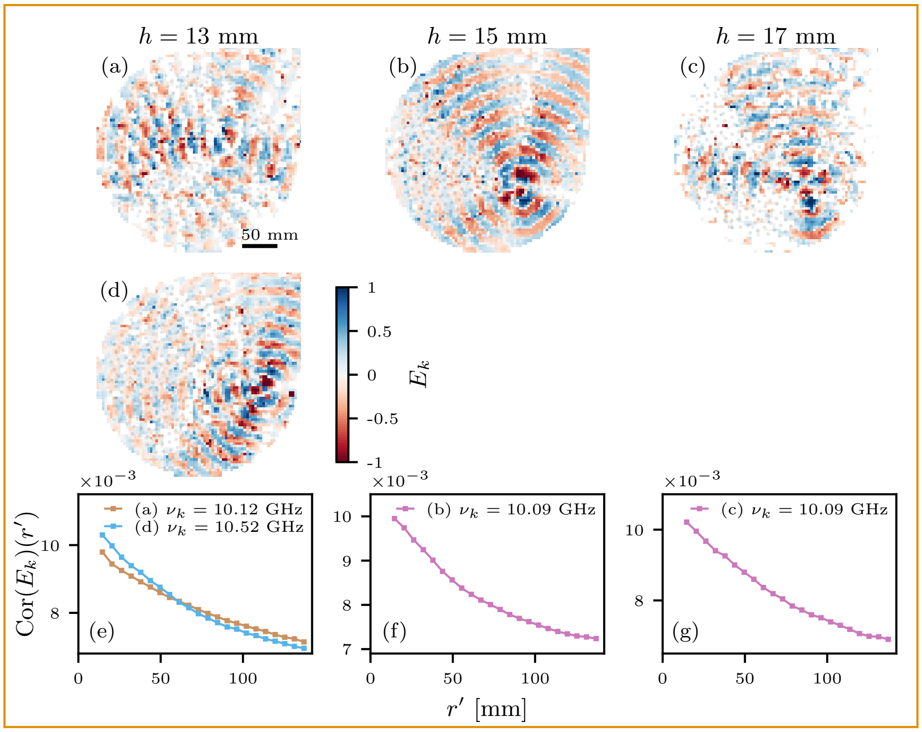

Fig. 10. [(a), (b), (c), and (d)] Spatial modal structure, and [(e), (f), and (g)] radial profile of the SA field (not shown) of representative eigenmodes found in the same GA spiral. Quality factors of the modes: (a) $Q_k = 2206$; (b) $Q_k = 2616$; (c) $Q_k = 2905$; (d) $Q_k = 4095$. Amplitude maps are normalized such that $\max(|E_k|) = 1$, thus $\max(|\mathrm{Cor}(E_k)|) = 1$. Radial decays are obtained by performing an angular average in the autocorrelation space (r' is measured from the well defined autocorrelation center).

spacing much smaller than the modal width) obliterates DoS details, thus making eigenstate reconstruction impossible.

4.2. Disordered system

Figures 8(b), (d), and (f) depict the distribution of the quality factors extracted for DS lattice. At low frequency (ν<8.8 GHz), the behaviour of Q_k is similar to the one presented by the GA spiral, *i.e.*, the quality factors go from values close to zero at $\nu \sim 8$ GHz to a maximum at $\nu \sim 8.7$ GHz. Likewise, the DoS curves are quite similar to each other being only differentiated by their intensity. As explained before, this difference is given by the coupling of the antenna to the electromagnetic field. However, a difference between the two structures, GA spiral and DS lattice, can be observed by reconstructing in real space some typical eigenstates carried by the DS and comparing them with those previously depicted in the GA. Figures 12(a), (b), and (c) present three modes with frequencies $\nu_k \sim 8.3$ GHz at different heights h. Given the lack of a geometrical center in disordered structures, radial decay functions are only achieved by means of the SA (not shown) and are depicted in Figs. 12(m), (n), and (o) [purple lines]. As expected for a 2D disordered system, this analysis leads to exponential radial decays in all three cases. Low frequency states ($\nu \sim 8.3$ GHz) with $\xi_{\mathrm{loc}} \sim 200$ mm reach the boundaries of the structure and subsequently leak, giving rise to poor quality factors.

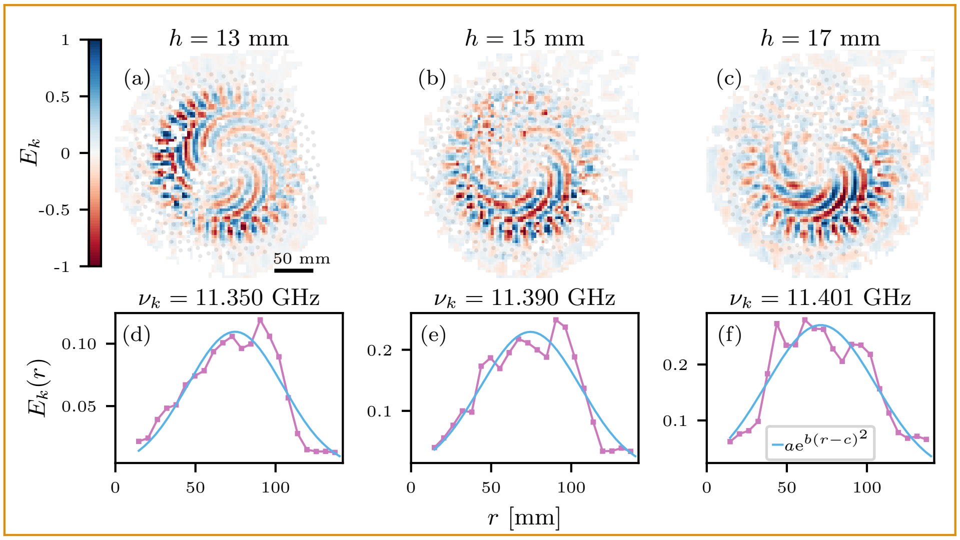

Fig. 11. Spatial modal structure [and corresponding radial profile] of representative Gaussian eigenmodes with characteristic quality factor (a) $Q_k \approx 5170$, (b) $Q_k \approx 4846$, and (c) $Q_k \approx 4159$. Amplitude maps are normalized such that $\max(|E_k|) = 1$. Radial decays (pink dots) are obtained by performing an azimuthal average operation where $r = \sqrt{(x+5)^2 + y^2}$, *i.e.*, r is measured from the geometrical center of the spiral and expressed in mm.

As confirmed by the DoS curves in Fig. 8(h), quality factor maps show the disappearance of the first bandgap observed for the GA spiral (8.5 GHz<ν<9.1 GHz). The unpopulated regions corresponding to the bandgaps in the GA spiral are here rich in states, and the thin well-defined, defect peaks are broader for all h. The impact of the distance between plates is illustrated at $\nu \sim 9.1$ GHz, where well-spaced eigenmodes with high quality factors ($Q_k \sim 4000$) are found at $h = 13$ mm, while 3D states with lower quality factors ($Q_k \sim 3000$) emerge for $h = 15$ mm and $h = 17$ mm. At $\nu \sim 9.6$ GHz [see Fig. 12(f)], a huge reduction of Q_k is specially observed at $h = 17$ mm where $Q_k \rightarrow 0$.

Similarly to the GA spiral, the DoS curves display an increase of the number of modes with respect to h at $\nu \sim 9.2$ GHz ($h = 17$ mm) and $\nu \sim 9.6$ GHz ($h = 15$ mm) followed by a constant behaviour for all h values (10 GHz<ν<11 GHz). As previously, this tendency is related with 3D emerging states that compensate the decrease given by the coupling of the antenna to the field. In this frequency range, the quality factors present similar behaviours for all h with values between 1000 and 4000 until dropping to zero at $\nu \sim 10.7$ GHz. At highest energies (ν>11.5 GHz), an increment in the quality factors from zero to ~ 2000 is noticeable for all values of h. The biggest increment occurs for $h = 13$ mm, and is smaller for the other two heights. In this frequency range, a huge difference between the number of states carried by the structure at $h = 13$ mm against the cases $h = 15$ mm and $h = 17$ mm is also detected.

The spatial reconstruction of some eigenmodes are shown in Figs. 12 for [(d), (g), and (j)] $h = 13$ mm, [(e), (h), and (k)] $h = 15$ mm, and [(f), (i), and (l)] $h = 17$ mm. The corresponding radial decay of SA functions (the SA are not shown) are also depicted in Figs. 12(m)-(o). As expected, the analysis of the radial functions reveals a clear exponential decay in all presented cases, allowing to study the behavior of the localization length with respect to the frequency and the distance between plates. Our results reveal the presence of well-confined states ($\xi_{\text{loc}} \sim 50$ mm) with large quality factors ($Q_k \sim 3500$) around $\nu \sim 8.8$ GHz. Remarkably, this localized behaviour is robust against the change of h. In contrary to the GA spiral, no defect-like modes supported by

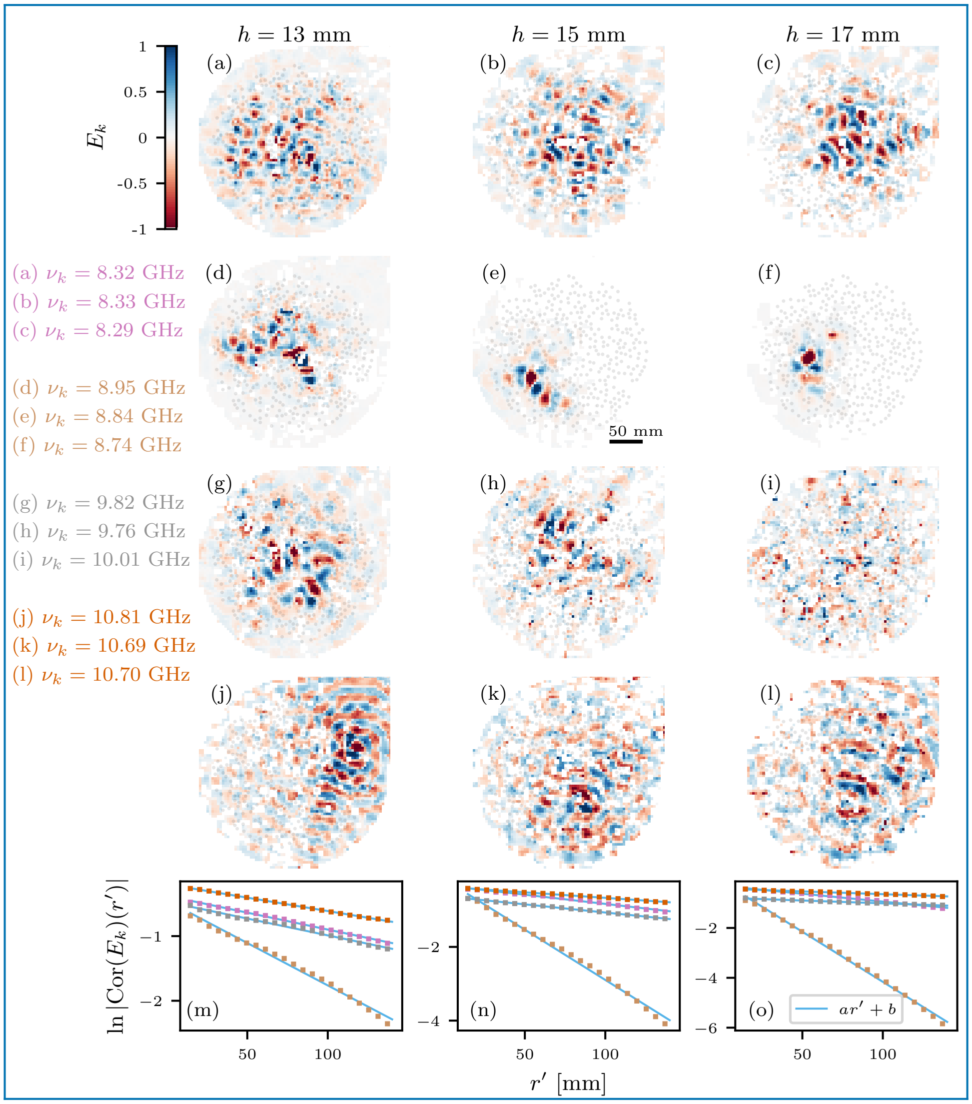

Fig. 12. [(a)-(l)] Spatial modal structure, and [(m)-(o)] radial profile of the field SA (not shown) of representative eigenmodes found in the same DS. States are characterised by quality factors, and localization lengths: (a) Q_k = 1479, $\xi_{\rm loc}$ = 195 mm; (b) Q_k = 1368, $\xi_{\rm loc}$ = 207 mm; (c) Q_k = 1117, $\xi_{\rm loc}$ = 165 mm; (d) Q_k = 3981, $\xi_{\rm loc}$ = 81 mm; (e) Q_k = 2542, $\xi_{\rm loc}$ = 40 mm; (f) Q_k = 4512, $\xi_{\rm loc}$ = 28 mm; (g) Q_k = 3596, $\xi_{\rm loc}$ = 196 mm; (h) Q_k = 3029, $\xi_{\rm loc}$ = 227 mm; (i) Q_k = 2541, $\xi_{\rm loc}$ = 436 mm; (j) Q_k = 2435, $\xi_{\rm loc}$ = 241 mm; (k) Q_k = 2671, $\xi_{\rm loc}$ = 337 mm; (l) Q_k = 2399, $\xi_{\rm loc}$ = 449 mm; Amplitude maps are normalized such that max($|E_k|$) = 1, thus max($|\mathrm{Cor}(E_k)|$) = 1. Radial decays are obtained by performing an angular average in the autocorrelation space (r' is measured from the well defined autocorrelation center).

only a couple of cylinders were detected all around the "bandgap" area (8.5 GHz<ν<9.1 GHz). The third and fourth rows of Fig. 12 shows modes with frequencies around $\nu \sim 10$ GHz and $\nu \sim 10.7$ GHz [last 2 red arrows in Figs. 8(b), (d), and (f)]. Due to the mixture of states, we observe a huge increase in the noise, in contrast with the states in the first row. Both rows display a steady increase in the localization length ξ_{loc} and a reduction in quality factor as a function of frequency and distance h. Note that at $\nu \sim 10$ GHz only the mode at $h = 13$ mm [Fig. 12(g)] can be considered quasi-localized ($\xi_{\text{loc}} = 196$ mm) while the others can easily reach the structure's boundaries and leak.

5. Conclusion

In the remarkably vivid domain of localization of electromagnetic waves, microwaves experiments play an important role in the understanding of how spatial correlations can enhance or halt transport [36]. In this paper, we use a well-controlled experimental setup consisting of microwaves propagating through lattices composed of dielectric Mie scatterers, in a metallic cavity of variable height. The simplicity of our platform allows us to efficiently study different kind of arrays such as disordered structures or aperiodic lattices with some hundreds of scatterers. Reflected and transmitted complex fields are detected and emitted by two straight antennas at the center of the structures and at the center of the top plate constituting the cavity. The cavity is mapped in frequency and space with a high degree of accuracy thanks to the VNA and to the fact of having a movable top plate and therefore a movable antenna. After the data acquisition, the density of states as well as the properties of the resonances of the system are extracted via the direct reflection measurement and the harmonic inversion/clustering methods applied to the transmission spectra. Another characteristic of this versatile experimental setup is the ability to control the distance between the two plates, thus breaking the translation invariance in the z-direction, and studying the wave propagation in the system beyond the pure 2D limit. Altogether we provide a full description of the experimental details that allowed us to experimentally demonstrate the existence of robust localization of microwaves reported in Ref. [19].

The above experimental setup allows us to investigate the resonance density and the corresponding quality factors as a function of two variables for two different systems: a traditional disordered lattice and a golden-angle Vogel spiral. By varying the frequency and the distance between both plates, we can investigate the behavior of the electromagnetic resonances as the system undergoes a 2D-3D crossover. Our findings reveal not only a huge difference in the shape of the eigenmodes corresponding to each structure and their radial decay, but also the robustness of Gaussian modes against varying the dimensionality of the cavity. This can be contrasted to disordered lattices, where eigenmodes always exhibit exponentially decreasing radial profiles, and typically are not spatially confined at high frequency where the cavities are not 2D anymore.

In summary, by providing a full description of the experimental setup to investigate microwave transport in Vogel spirals, we pave the way for a broader application of such structures to achieve electromagnetic localization in 3 dimensional dielectric media, which turns out to be very difficult in uncorrelated disordered systems [4,8].

Funding. CNPq, CAPES, and FAPERJ; Consejo Nacional de Ciencia y Tecnología (775585); UCAJEDI Investments in the Future project managed by the National Research Agency (ANR) (ANR_15_IDEX-01).

Acknowledgments. We thank L. Dal Negro, F. Sgrignuoli, M. Prado, and Y. Chen for enlightening discussions. F.A.P. acknowledge CNPq, CAPES, and FAPERJ for financial support. L.A.R.-L. gratefully acknowledges the financial support from CONACyT (Mexico), through the Grant No.775585, and from the French government, through the UCA$^{\text{JEDI}}$ Investments in the Future project managed by the National Research Agency (ANR) with the reference number ANR-15-IDEX-0001.

Disclosures. The authors declare no conflicts of interest.

Data availability. Data underlying the results presented in this paper are not publicly available at this time but may be obtained from the authors upon reasonable request.

References

1. P. W. Anderson, "Absence of diffusion in certain random lattices," Phys. Rev. **109**(5), 1492–1505 (1958).
2. E. Abrahams, P. W. Anderson, D. C. Licciardello, *et al.*, "Scaling theory of localization: Absence of quantum diffusion in two dimensions," Phys. Rev. Lett. **42**(10), 673–676 (1979).

3. P. W. Anderson, "The question of classical localization: a theory of white paint?" Philos. Mag. B **52**(3), 505–509 (1985).
4. T. Sperling, L. Schertel, M. Ackermann, *et al.*, "Can 3D light localization be reached in 'white paint'?" New J. Phys. **18**(1), 013039 (2016).
5. S. E. Skipetrov and I. M. Sokolov, "Absence of Anderson localization of light in a random ensemble of point scatterers," Phys. Rev. Lett. **112**(2), 023905 (2014).
6. J. Haberko, L. S. Froufe-Pérez, and F. Scheffold, "Transition from light diffusion to localization in three-dimensional amorphous dielectric networks near the band edge," Nat. Commun. **11**(1), 4867 (2020).
7. F. Scheffold, J. Haberko, S. Magkiriadou, *et al.*, "Transport through amorphous photonic materials with localization and bandgap regimes," Phys. Rev. Lett. **129**(15), 157402 (2022).
8. A. Yamilov, S. E. Skipetrov, T. W. Hughes, *et al.*, "Anderson localization of electromagnetic waves in three dimensions," Nat. Phys. **19**(9), 1308–1313 (2023).
9. C. E. Máximo, N. Piovella, P. W. Courteille, *et al.*, "Spatial and temporal localization of light in two dimensions," Phys. Rev. A **92**(6), 062702 (2015).
10. L. S. Froufe-Pérez, M. Engel, J. J. Sáenz, *et al.*, "Band gap formation and Anderson localization in disordered photonic materials with structural correlations," Proc. Natl. Acad. Sci. **114**(36), 9570–9574 (2017).
11. R. A. Vicencio, C. Cantillano, L. Morales-Inostroza, *et al.*, "Observation of localized states in Lieb photonic lattices," Phys. Rev. Lett. **114**(24), 245503 (2015).
12. S. Mukherjee, A. Spracklen, D. Choudhury, *et al.*, "Observation of a localized flat-band state in a photonic Lieb lattice," Phys. Rev. Lett. **114**(24), 245504 (2015).
13. P. Wang, Y. Zheng, X. Chen, *et al.*, "Localization and delocalization of light in photonic moiré lattices," Nature **577**(7788), 42–46 (2020).
14. F. Sgrignuoli, R. Wang, F. A. Pinheiro, *et al.*, "Localization of scattering resonances in aperiodic Vogel spirals," Phys. Rev. B **99**(10), 104202 (2019).
15. L. Dal Negro, R. Wang, and F. A. Pinheiro, "Structural and spectral properties of deterministic aperiodic optical structures," Crystals **6**(12), 161 (2016).
16. J. Trevino, H. Cao, and L. Dal Negro, "Circularly symmetric light scattering from nanoplasmonic spirals," Nano Lett. **11**(5), 2008–2016 (2011).
17. L. Dal Negro, N. Lawrence, and J. Trevino, "Analytical light scattering and orbital angular momentum spectra of arbitrary Vogel spirals," Opt. Express **20**(16), 18209–18223 (2012).
18. A. Christofi, F. A. Pinheiro, and L. Dal Negro, "Probing scattering resonances of Vogel's spirals with the Green's matrix spectral method," Opt. Lett. **41**(9), 1933–1936 (2016).
19. L. A. Razo-López, G. J. Aubry, F. A. Pinheiro, *et al.*, "Strong localization of microwaves beyond two dimensions in aperiodic Vogel spirals," Phys. Rev. B **109**(1), 014205 (2024).
20. L. S. Froufe-Pérez, M. Engel, P. F. Damasceno, *et al.*, "Role of short-range order and hyperuniformity in the formation of band gaps in disordered photonic materials," Phys. Rev. Lett. **117**(5), 053902 (2016).
21. C. Bohren and D. Huffman, *Absorption and Scattering of Light by Small Particles*, Wiley Science Series (Wiley, 2008).
22. H. C. van de Hulst, *Light Scattering by Small Particles*, Dover Books on Physics (Dover Publications, 1981).
23. G. J. Aubry, L. S. Froufe-Pérez, U. Kuhl, *et al.*, "Experimental tuning of transport regimes in hyperuniform disordered photonic materials," Phys. Rev. Lett. **125**(12), 127402 (2020).
24. J. Barthélemy, O. Legrand, and F. Mortessagne, "Complete *S* matrix in a microwave cavity at room temperature," Phys. Rev. E **71**(1), 016205 (2005).
25. M. R. Wall and D. Neuhauser, "Extraction, through filter-diagonalization, of general quantum eigenvalues or classical normal mode frequencies from a small number of residues or a short-time segment of a signal. I. Theory and application to a quantum-dynamics model," J. Chem. Phys. **102**(20), 8011–8022 (1995).
26. V. A. Mandelshtam and H. S. Taylor, "Spectral analysis of time correlation function for a dissipative dynamical system using filter diagonalization: Application to calculation of unimolecular decay rates," Phys. Rev. Lett. **78**(17), 3274–3277 (1997).
27. V. A. Mandelshtam and H. S. Taylor, "Harmonic inversion of time signals and its applications," J. Chem. Phys. **107**(17), 6756–6769 (1997).
28. L. C. Maier and J. C. Slater, "Field Strength Measurements in Resonant Cavities," J. Appl. Phys. **23**(1), 68–77 (1952).
29. C. Ruiz, M. Spiliopoulou, and E. Menasalvas, "C-DBSCAN: Density-based clustering with constraints," in *Rough Sets, Fuzzy Sets, Data Mining and Granular Computing*, A. An, J. Stefanowski, S. Ramanna, C. J. Butz, W. Pedrycz, and G. Wang, eds. (Springer Berlin Heidelberg, Berlin, Heidelberg, 2007), pp. 216–223.
30. H. Ishio, A. I. Saichev, A. F. Sadreev, *et al.*, "Wave function statistics for ballistic quantum transport through chaotic open billiards: Statistical crossover and coexistence of regular and chaotic waves," Phys. Rev. E **64**(5), 056208 (2001).
31. E. Akkermans and G. Montambaux, *Mesoscopic Physics of Electrons and Photons* (Cambridge University Press, 2007).
32. M. Reisner, Y. Tahmi, F. Piéchon, *et al.*, "Experimental observation of multifractality in Fibonacci chains," Phys. Rev. B **108**(6), 064210 (2023).
33. M. Reisner, "Experimental studies of multifractality and topological phase transitions in microwave resonator lattices," PhD thesis, Université Côte d'Azur (2023).

34. D. Laurent, O. Legrand, P. Sebbah, *et al.*, “Localized modes in a finite-size open disordered microwave cavity,” Phys. Rev. Lett. **99**(25), 253902 (2007).
35. S. F. Liew, H. Noh, J. Trevino, *et al.*, “Localized photonic band edge modes and orbital angular momenta of light in a golden-angle spiral,” Opt. Express **19**(24), 23631–23642 (2011).
36. K. Vynck, R. Pierrat, R. Carminati, *et al.*, “Light in correlated disordered media,” Rev. Mod. Phys. **95**(4), 045003 (2023).